NANO LETTERS
Letter
Cite This: Nano Lett. 2019, 19, 4180−4187
pubs.acs.org/NanoLett

# Advanced One- and Two-Dimensional Mesh Designs for Injectable Electronics

Robert D. Viveros,[†,⊥] Tao Zhou,[‡,⊥] Guosong Hong,[‡] Tian-Ming Fu,[‡] Hao-Yu Greg Lin,[§] and Charles M. Lieber*[,†,‡,∥]

[†]John A. Paulson School of Engineering and Applied Sciences, [‡]Department of Chemistry and Chemical Biology, [§]Center for Nanoscale Systems, and [∥]Center for Brain Science, Harvard University, Cambridge, Massachusetts 02138, United States

Supporting Information

**ABSTRACT:** The unique structure and mechanical properties of syringe-injectable mesh electronics have enabled seamless tissue integration and stable chronic recording of the activities of the same neurons on a year scale. Here, we report studies of a series of structural and mechanical mesh electronics design variations that allow injection using needles at least 4-fold smaller than those previously reported to minimize the footprint during injection of the electronics in soft matter and tissue. Characterization of new ultraflexible two-dimensional (2D) and one-dimensional (1D) probes has demonstrated reproducible injection of the newly developed mesh electronics designs via needles as small as 100 $\mu$m in inner diameter (ID) with reduced injection volumes. *In vitro* hydrogel and *in vivo* mouse brain studies have shown that ultraflexible 2D and 1D probes maintain their structural integrity and conformation post-injection after being transferred through the reduced diameter needles. In addition, analysis of the variation of the post-injection mesh cross sections suggests a smaller degree of tissue deformation and relaxation with decreasing needle diameters. The capability to implement rational design for mesh electronic probes that can be delivered via much smaller diameter needles should open up new opportunities for integration of electronics with tissue and soft matter in fundamental and translational studies.

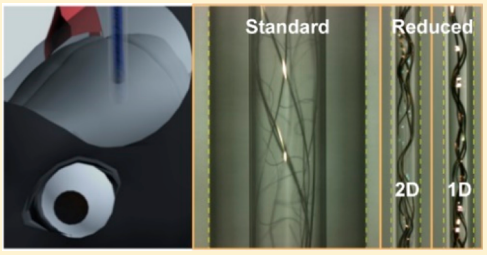


**KEYWORDS:** *Tissue-like electronics, ultrasmall needle, minimal footprint, ultraflexible probe, one-dimensional probe, soft material integration*



Integrating electronic probes into synthetic and natural soft materials provides the opportunity to monitor dynamic behavior through and deep within these structures.[1−8] Microwire[9,10] and silicon probes[11,12] can be mechanically inserted in a controlled manner into soft materials and, in the case of the brain, can offer superior spatiotemporal resolution compared to surface probes[13−19] and imaging modalities,[20,21] independent of depth. Despite these advantages, such implantable probes generally have substantial mechanical and other mismatches with soft materials that hinder stable integration.[22−25] In the case of the brain, the mechanical and structural mismatches with neural tissue lead to a chronic immune response, which results in a buildup of glial cells immediately adjacent to the probe surface, and micromotion that together make single-neuron tracking over extended periods of time difficult, if not impossible.[24−26]

Mesh electronics offer a novel paradigm of implantable soft electronics with brain-like structure and mechanics, which circumvent issues associated with conventional approaches.[27−33] The unique macroporous topology with submicrometer thickness and cell soma-scale width mesh elements allow for stable and seamless tissue integration by virtue of their unique mechanical and structural properties.[27,29,30] Previous studies of mesh electronics have demonstrated stable chronic recording from the same individual neurons for at least 8 months,[29] and more recent work has demonstrated opportunities for substantially increased multiplexity[32] as well as efficient interfacing with external electronic systems.[31] The macroporous mesh electronics platform has also achieved seamless interfacing with other soft materials, including (1) collagen, alginate, and PLGA fibrous scaffolds,[1] (2) organic gels and polymers,[2] and (3) the first interface with the retinal ganglion cell layer of the mouse eye capable of awake chronic recording.[33]

While these previous studies have validated the unique three-dimensional (3D) integration of mesh electronics with different soft materials, challenges related to delivery still exist. Due to the high intrinsic flexibility of the probe that precludes direct insertion, syringe injection, similar to standard pharmaceutical administration, has been used as a flexible method for implantation of mesh electronic probes into target materials.[27] Previous studies have focused on relatively large 400 $\mu$m inner diameter (ID)/550 $\mu$m[34] to 650 $\mu$m[28−32] outer diameter (OD) needles to allow for smooth injection of the probes into brain tissue given their structural and mechanical properties. These relatively large needles can produce an acute

**Received:** April 26, 2019
**Revised:** May 9, 2019
**Published:** May 10, 2019





DOI: 10.1021/acs.nanolett.9b01727
Nano Lett. 2019, 19, 4180−4187

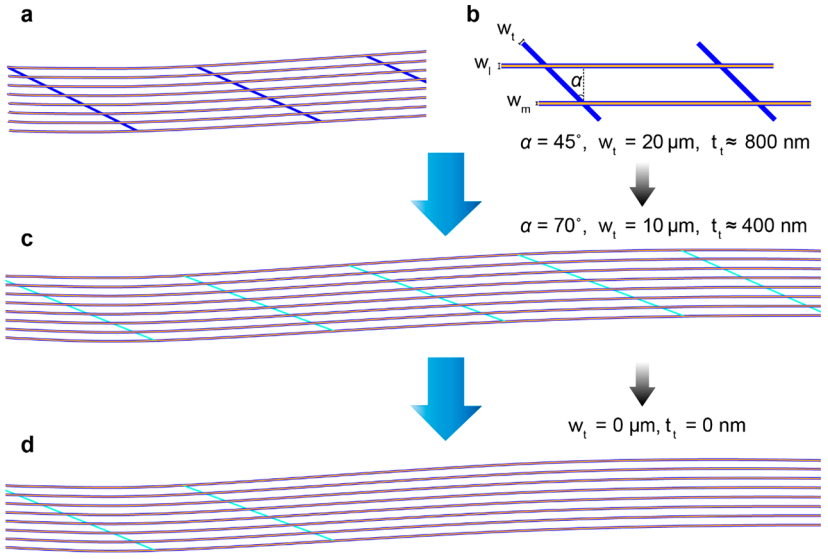


**Figure 1.** Structural design of ultraflexible syringe-injectable mesh electronics. (a) Schematic of a conventional mesh electronics probe. (b) Schematic of the mesh electronics unit cell, highlighting key probe design parameters, including the angle between longitudinal and transverse elements ($\alpha$), the longitudinal element width ($w_l$), the transverse element width ($w_t$), the longitudinal interconnect metal width ($w_m$), and the transverse element thickness ($t_t$) for the previous standard mesh ($\alpha$ = 45°, $w_l$ = 20 $\mu$m, $w_t$ = 20 $\mu$m, $w_m$ = 10 $\mu$m, and $t_t \approx$ 800 nm). (c) Schematic of ultraflexible 2D mesh electronics to facilitate loading and injection using reduced diameter needles and injection volumes, where $\alpha$ = 70°, $w_t$ = 10 $\mu$m, and $t_t \approx$ 400 nm; parameters for the longitudinal elements are the same as in the standard design highlighted in panel b. (d) Schematic of ultraflexible 1D mesh electronics with transverse element removal in the implantation site, such that $w_t$ and $t_t$ equal zero, and parameters for the longitudinal elements and transverse elements external to the implantation region are the same as those of the 2D probe highlighted in panel c. Orange represents the Au interconnects, dark blue two SU-8 layers for interconnect insulation, and cyan a single SU-8 layer.

disturbance of the local tissue,[30] although studies to date have demonstrated tissue healing following implantation without the foreign body/immune response found for more rigid probes. Exploring further the acute impact of these relatively large needles and simultaneously determining diameter limits of smaller delivery needles require innovation in the structural and mechanical design to improve the flexibility of the mesh electronics. Herein, we present systematic studies that demonstrate new two-dimensional (2D) and one-dimensional (1D) mesh electronics designs with reduced and vanishing transverse bending stiffness ($D_t$) values, respectively, that allow high-yield controlled low-volume injection via 100 $\mu$m ID glass needles into representative synthetic and biological soft materials.

To enable the use of reduced diameter needles for probe implantation, we first assessed the mechanical properties of the mesh electronics for different structural configurations. Key points related to the standard mesh electronics design are highlighted in panels a and b of Figure 1. First, standard mesh electronics probes have periodic structures that can be defined using a unit cell (Figure 1a,b). In the unit cell of the mesh, we define longitudinal elements parallel to the injection direction and transverse elements oriented at angle $\alpha$ of 45° relative to the longitudinal direction (Figure 1b).[28−32] Second, the longitudinal elements are composite structures, consisting of gold (Au) interconnects that are sandwiched by two layers of biocompatible photoresist SU-8.[35] The longitudinal elements terminate at one end with sensor or stimulation devices, such as metal electrodes[4,27−31] or nanowire transistors,[1,2,4,27] and at the opposite end with input/output (I/O) pads that remain external to the target material and are used to interface to external electronics. Third, the transverse elements consist of two SU-8 layers with a total thickness of approximately 800 nm and a width of 20 $\mu$m. The transverse elements determine the $D_t$ of the overall mesh structure and, correspondingly, how readily mesh probes roll up when loaded into needles.[27] Lastly, both longitudinal and transverse elements contribute to the longitudinal bending stiffness ($D_l$) of the mesh probes, where a sufficiently large $D_l$ helps to maintain the overall linear structure during injection.[27,28] Therefore, our focus in this study was to reduce $D_t$ while maintaining an approximately constant $D_l$ for the different probe designs.

To explore how key design parameters affected $D_t$ and $D_l$, we investigated (i) relative angle $\alpha$ between longitudinal and transverse elements, (ii) total transverse element thickness $t_t$, and (iii) transverse element width $w_t$. Ultraflexible 2D mesh electronics designs with increases in $\alpha$ to 70°, where $\alpha$ = 0° defines a rectangular unit cell, as well as decreases in $w_t$ and $t_t$ by factors of 2 to 10 $\mu$m and 400 nm, respectively, were studied (Figure 1c). We also considered a 1D structural region by investigating the impact of removing the transverse elements, corresponding to $w_t$ = 0 $\mu$m and $t_t$ = 0 nm, from the implanted portion of the probe (Figure 1d). Other design parameters remained unchanged relative to the standard design paradigm, with $w_l$ = 20 $\mu$m, $w_m$ = 10 $\mu$m, and longitudinal interconnect metal thickness $t_m$ = 105 nm.

We used finite element analysis (FEA) of the mesh electronics unit cell (Materials and Methods in the Supporting Information)[27,30,32] to quantify the impact of these design variations on probe stiffness. Simulations were performed on probe unit cells with $\alpha$ values between 0° and 70°, a $w_t$ of 20 or 10 $\mu$m, and a $t_t$ of ≈800 or ≈400 nm. These results are summarized in panels a and b of Figure 2 and highlight several key points. $D_t$ of the 2D mesh electronics decreased substantially with an increase in $\alpha$, a decrease in $w_t$, and most notably a decrease in $t_t$ with other design parameters fixed (Figure 2a). Increasing $\alpha$ from 0° to the standard value of 45° with fixed values of $w_t$ and $t_t$ reduced $D_t$ by ∼30%;



DOI: 10.1021/acs.nanolett.9b01727
Nano Lett. 2019, 19, 4180−4187

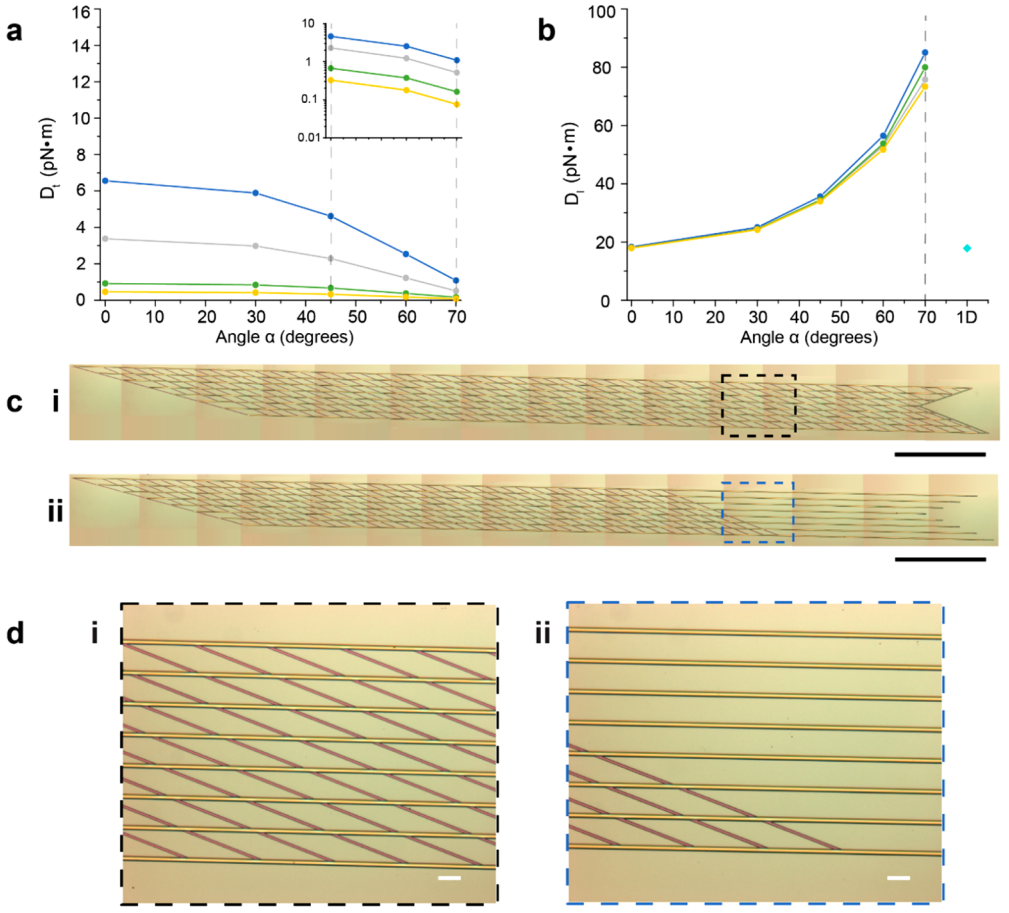


**Figure 2.** Analysis and fabrication of advanced mesh electronics designs. (a) $\alpha$ dependence of $D_t$ determined using FEA of the mesh electronics unit cell. The four analyzed transverse element dimension parametrizations were as follows: for the blue curve, $w_t$ = 20 $\mu$m and $t_t \approx$ 800 nm; for the green curve, $w_t$ = 20 $\mu$m and $t_t \approx$ 400 nm; for the gray curve, $w_t$ = 10 $\mu$m and $t_t \approx$ 800 nm; and for the yellow curve, $w_t$ = 10 $\mu$m and $t_t \approx$ 400 nm. The inset shows a log-scale plot of the $\alpha$ dependence of $D_t$ between 45° and 70°. (b) $\alpha$ dependence of $D_l$ determined using FEA of the mesh electronics unit cell. The same four transverse element parametrizations were analyzed from panel a, using the same color scheme, in addition to the design in which $w_t$ = 0 $\mu$m and $t_t$ = 0 nm (1D probe; cyan diamond). (c) Tiled bright-field optical microscopy images of fabricated ultraflexible 2D (i) and 1D (ii) mesh electronics with $w_t$ = 10 $\mu$m and $t_t \approx$ 400 nm. Scale bars are 2 mm. (d) Bright-field optical microscopy images of corresponding outlined regions from panel c of 2D (i) and 1D (ii) mesh electronics. Scale bars are 100 $\mu$m.

importantly, further increasing $\alpha$ from 45° to 70° resulted in an ~75% decrease in $D_t$. Furthermore, with fixed $t_t$ and $\alpha$, reducing $w_t$ in half (from the blue curve to the gray curve for $t_t \approx$ 800 nm or from the green curve to the yellow curve for $t_t \approx$ 400 nm) generally reduced $D_t$ by ~50%. In addition, halving $t_t$ with fixed values of $\alpha$ and $w_t$ (from the blue curve to the green curve for $w_t$ = 20 $\mu$m or from the gray curve to the yellow curve for $w_t$ = 10 $\mu$m) produced the most significant reduction in $D_t$ of ~85%. Significantly, the simulations demonstrate that these design variations can yield a ~60-fold reduction in $D_t$ (0.08 pN·m, yellow curve at $\alpha$ = 70°), compared to the previous standard design[28−31] (4.6 pN·m, blue curve at $\alpha$ = 45°).

The longitudinal bending stiffness, $D_l$, was also assessed for the same 2D probe designs (Figure 2b). For a given transverse element dimension set, increases in $\alpha$ from 0° to 45° and from 45° to 70° yielded $D_l$ increases of ~90% and ~115−140%, respectively. For modification of the transverse element dimensions, $D_l$ was reduced by ~5% from the design in which $w_t$ = 20 $\mu$m and $t_t \approx$ 800 nm (blue curve) to the design in which $w_t$ = 10 $\mu$m and $t_t \approx$ 400 nm (yellow curve) with $\alpha$ = 45°; the reduction was ~15% with $\alpha$ = 70° between those designs. The minor reduction in $D_l$ with reduced transverse element dimensions suggests that these design components contribute minimally to $D_l$ for the examined $\alpha$. On the other hand, increasing $\alpha$ increases the stiffness contribution from the transverse elements in the longitudinal direction, which would expectedly increase $D_l$. In addition, $D_l$ of the implanted portion of the 1D probes (Figure 2b, blue diamond) was roughly identical to that of the various 2D $\alpha$ = 0° designs; that is, for a rectangular ($\alpha$ = 0°) cell, the transverse elements provide effectively no contribution to $D_l$, behaving like the 1D designs. It should be noted that while the unit cell does exhibit increases in $D_l$ for several designs (Figure 2b), the stiffness of each individual longitudinal element per unit width remains constant for these design variations because the geometrical cross section of these elements is unchanged.[30]

To explore experimentally the consequences of these design variations, we fabricated new 2D and 1D mesh electronics probes using standard photolithography procedures as previously reported (Materials and Methods in the Supporting Information).[27−33] Briefly, the bottom SU-8 layer mesh structure was patterned on a silicon wafer coated with a sacrificial nickel (Ni) layer. Next, the Au interconnects and platinum (Pt) sensor electrodes were patterned and deposited in sequential steps. Lastly, the top SU-8 layer of the mesh structure, which encapsulates and insulates the interconnects



DOI: 10.1021/acs.nanolett.9b01727
Nano Lett. 2019, 19, 4180−4187

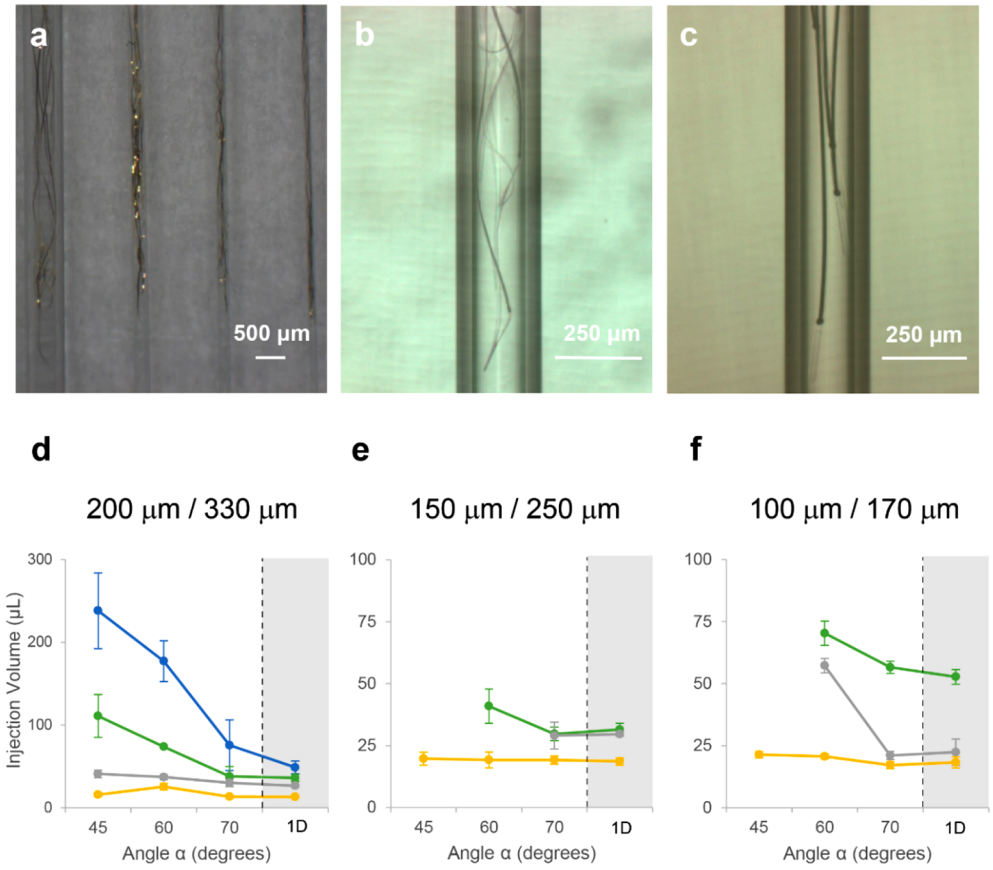


**Figure 3.** *In vitro* loading and injection of mesh electronics using reduced diameter needles. (a) Photograph of the lowest-$D_t$ 2D mesh electronics probe loaded within 400 $\mu$m/650 $\mu$m, 200 $\mu$m/330 $\mu$m, 150 $\mu$m/250 $\mu$m, and 100 $\mu$m/170 $\mu$m ID/OD glass capillary needles from left to right, respectively. (b) Bright-field microscopy image of the lowest-$D_t$ 2D mesh electronics loaded into a 150 $\mu$m/250 $\mu$m glass needle. (c) Bright-field microscopy image of a 1D mesh probe, which has a 2D structure similar to that in panel b, loaded into a 150 $\mu$m/250 $\mu$m glass needle. PBS injection volume for complete mesh ejection using (d) 200 $\mu$m/330 $\mu$m, (e) 150 $\mu$m/250 $\mu$m, and (f) 100 $\mu$m/170 $\mu$m glass capillary needles for mesh designs that were successfully loaded in the different needles. The design parameters are as follows: for the blue curve, $w_t$ = 20 $\mu$m and $t_t \approx$ 800 nm; for the green curve, $w_t$ = 10 $\mu$m and $t_t \approx$ 800 nm; for the gray curve, $w_t$ = 20 $\mu$m and $t_t \approx$ 400 nm; and for the yellow curve, $w_t$ = 10 $\mu$m and $t_t \approx$ 400 nm. The 1D mesh electronics have a 4 mm long 1D region, and the remaining portion of the structure is a 2D mesh, where the parameters are kept the same as those of the $\alpha$ = 70° probe of the corresponding 2D design.

while keeping the sensor electrodes and I/O pads exposed, was patterned.

Probes were characterized by optical microscopy prior to being released from the substrate. A tiled image that provides a view of the entire structure of the lowest-$D_t$ 2D design ($\alpha$ = 70°, $w_t$ = 10 $\mu$m, and $t_t \approx$ 400 nm) shows the contiguous mesh structure with good alignment of distinct layers and regions (Figure 2c, i), including the I/O pads for electrical interfacing at the left side (zoom, Figure S1a) and sensor electrodes at the right side (zoom, Figure S1b). A tiled image of a 1D probe (Figure 2c, ii) shows features similar to those of the 2D design, including I/O pads for electrical interfacing at the left side (Figure S1c), as well as the absence of transverse elements at the right side containing the electrode sensor elements (Figure 2c, ii, and Figure S1d). Higher-resolution images (Figure 2d) comparing the 2D/1D transition region in the 1D mesh and same position in the full 2D mesh (Figure 2c, blue and black dashed boxes, respectively) highlight the removal of transverse mesh elements that is expected to minimize transverse constraints on the 1D sensing element region once implanted into a soft material.

We first investigated loading and injection of the new 2D and 1D mesh design as a function of capillary needle ID to determine the practical mechanical flexibility and suitability for syringe-based injection into soft materials (Figure 3). Fabricated mesh electronics probes were released from substrates by etching the sacrificial Ni layer, washed in deionized (DI) water, and then suspended in 1× phosphate-buffered saline (PBS) (Materials and Methods in the Supporting Information). Optical images (Figure 3a) show that the lowest-$D_t$ design ($\alpha$ = 70°, $w_t$ = 10 $\mu$m, and $t_t \approx$ 400 nm) could be successfully loaded within 400 $\mu$m/650 $\mu$m, 200 $\mu$m/330 $\mu$m, 150 $\mu$m/250 $\mu$m, and 100 $\mu$m/170 $\mu$m ID/OD glass needles. Close examination of these images (Figure 3b and Figure S2a–c) shows that the lowest-$D_t$ 2D mesh probes are loaded with linear elongated conformations, without apparent compression, in the reduced diameter needles. The 1D probe, which has the lowest-$D_t$ design for its 2D region, exhibited a similar linear conformation in the reduced diameter needles (Figure 3c and Figure S2d–f), illustrating that the 2D and 1D probes demonstrate similar in-needle loading behavior. These results demonstrate facile loading in substantially smaller diameter injection needles compared to previous studies in which 400 $\mu$m/650 $\mu$m[28−32] and 400 $\mu$m/550 $\mu$m[34] needles were used.



DOI: 10.1021/acs.nanolett.9b01727
*Nano Lett.* 2019, 19, 4180−4187

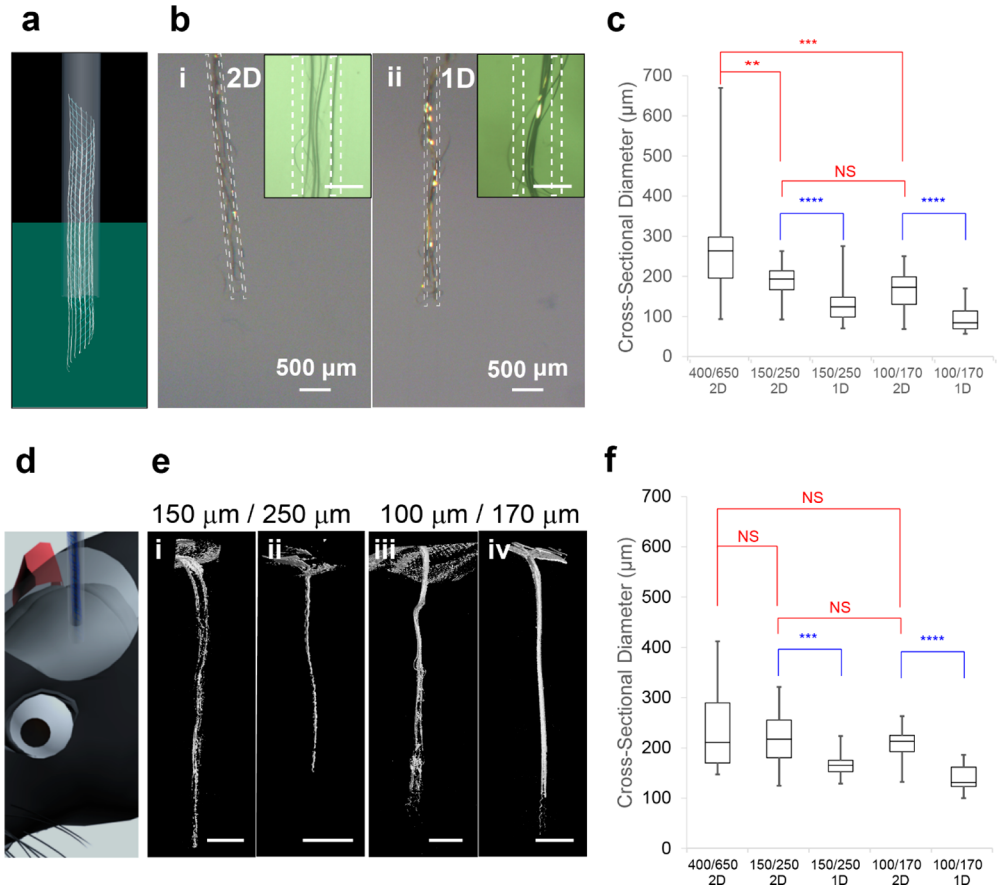


**Figure 4.** Injection of mesh electronics into tissue and tissue-like media. (a) Schematic representation of the injection of mesh electronics into hydrogel. (b) Photomicrographs of 2D (i) and 1D (ii) probes injected into 0.5% agarose hydrogel using 150 $\mu$m/250 $\mu$m ID/OD glass needles. Insets are of separate injections, and needle dimensions are represented by dashed white boxes. Inset scale bars are 200 $\mu$m. (c) Cross-sectional diameters of the 2D and 1D mesh electronics injected into 0.5% agarose hydrogel vs capillary needle ID/OD with numbers in micrometers. The diameters were obtained from direct measurement of bright-field microscopy images. (d) Schematic representation of the injection of mesh electronics into a mouse brain. (e) Micro-CT images of 2D (i and iii) and 1D (ii and iv) mesh electronics injected into a mouse brain such that one of each probe type was injected using both 150 $\mu$m/250 $\mu$m (i and ii) and 100 $\mu$m/170 $\mu$m (iii and iv) glass needles. Scale bars are 500 $\mu$m. The mouse brains with implanted mesh probes were fixed at 1 h post-implantation (Materials and Methods in the Supporting Information). (f) Cross-sectional diameters of ultraflexible 2D and 1D mesh electronics injected into a mouse brain using several distinct glass needle sizes. All injections were performed using the lowest-$D_t$ 2D and 1D mesh probes. The red and blue indicate $P$ values for 2D vs 2D and 2D vs 1D measurements, respectively, where NS (not significant) indicates $P > 0.05$, two asterisks indicate $P < 0.01$, three asterisks indicate $P < 0.001$, and four asterisks indicate $P < 0.0001$ (by a two-tailed $t$ test).

Next, we asked how the total solution volume required to fully eject mesh probes from capillary needles varies as a function of the different mesh design parameters and needle ID. First, data acquired from studies of 2D probes with the four basic structural designs ($w_t$ and $t_t$) for angles $\alpha$ of 45°, 60°, and 70°, in addition to 1D probes with 2D regions corresponding to the four basic structures at $\alpha$ = 70°, injected through 200 $\mu$m/330 $\mu$m ID/OD needles (Figure 3d) show several key points. Overall, the data show that all designs could be reproducibly ejected from 200 $\mu$m ID needles, although the total volumes varied over an order of magnitude. Increasing $\alpha$ or decreasing $w_t$ or $t_t$ generally reduced the injection volume. The standard transverse element dimensions (for the blue curve, $w_t$ = 20 $\mu$m and $t_t \approx$ 800 nm) demonstrated a reduction in injection volume from ~240 to 75 $\mu$L when $\alpha$ increased from 45° to 70°. The injection volume was further reduced to ~15 $\mu$L with $w_t$ = 10 $\mu$m and $t_t \approx$ 400 nm designs (yellow curve) for all values of $\alpha$, where the $\alpha$ dependence became less impactful for reduced $w_t$ and $t_t$. Lastly, the 1D probe designs exhibited injection volumes similar to or slightly smaller than the corresponding 70° $\alpha$ values for each of the four basic structural ($w_t$ and $t_t$) designs.

Importantly, several of the more flexible/lower-$D_t$ designs also enabled reproducible injection through substantially smaller diameter needles (Figure 3e,f). For 150 $\mu$m ID needles (Figure 3e), the $w_t$ = 20 $\mu$m, $t_t \approx$ 800 nm designs (blue curve, Figure 3d) could not be reproducibly loaded for values of $\alpha$ from 45° to 70°. However, reducing $w_t$ to 10 $\mu$m (green curve) allowed for reliable probe loading and yielded injection volumes of ~40 and ~30 $\mu$L for $\alpha$ values of 60° and 70°, respectively. Additionally, reducing $t_t$ in half allowed for reproducible probe injection using 30 $\mu$L with a $w_t$ of 20 $\mu$m ($\alpha$ = 70°, gray curve) and 20 $\mu$L with a $w_t$ of 10 $\mu$m ($\alpha$ = 45°, 60°, and 70°, yellow curve). The corresponding 1D probe designs exhibited injection volumes similar to those of the corresponding 70° $\alpha$ values for each of the basic structural ($w_t$ and $t_t$) designs.

Notably, the more flexible/lower-$D_t$ designs also enabled reproducible injection through 100 $\mu$m ID needles (Figure 3f), which have IDs 4-fold smaller than those in our previous work.



DOI: 10.1021/acs.nanolett.9b01727
Nano Lett. 2019, 19, 4180−4187

While the $w_t$ = 20 $\mu$m, $t_t \approx$ 800 nm designs (blue curve, Figure 3d) could not be loaded for any value of $\alpha$, reducing $w_t$ in half (green curve) permitted loading and ejection with volumes of ~70 and ~55 $\mu$L for $\alpha$ values of 60° and 70°, respectively. Reducing $t_t$ to ~400 nm enabled ejection of the $w_t$ = 20 $\mu$m designs (gray curve) using volumes of ~55 and ~20 $\mu$L for $\alpha$ values of 60° and 70°, respectively, and also reducing $w_t$ to 10 $\mu$m (yellow curve) allowed for injection using a volume of ~20 $\mu$L for $\alpha$ values from 45° to 70°. The 1D probe designs exhibited injection volumes similar or slightly smaller than those of the corresponding 70° $\alpha$ values for each of these basic structural ($w_t$ and $t_t$) designs. Together, these results demonstrate that rationally designed mesh electronics with a reduced $D_t$ can enable controlled and reproducible loading into and ejection through capillary needles with an ID ≤4-fold smaller than those in our previous work. Lastly, the injection volume in the optimal designs, 10−25 $\mu$L, is smaller than in prior studies using the larger 400 $\mu$m ID needles.[28,29,31]

We investigated injection into nonliving and living soft materials to characterize the post-injection conformations of ultraflexible 2D and 1D mesh electronics as a function of capillary needle size. The lowest-$D_t$ 2D and 1D probes ($\alpha$ = 70°, $w_t$ = 10 $\mu$m, and $t_t \approx$ 400 nm) were implanted using a field-of-view (FoV) injection methodology[28] to a depth of 4 mm (Figure 4a−c) into 0.5% (w/v) agarose hydrogel that is a good mimic of dense brain tissue with similar Young's and shear moduli[36,37] (Materials and Methods in the Supporting Information). Optical images of 2D (Figure 4b, i) and 1D (Figure 4b, ii) probes implanted using 150 $\mu$m/250 $\mu$m ID/OD capillary needles yielded notable differences in overall conformation. Specifically, the 2D mesh probe appeared to be confined within the initial insertion region defined by the needle OD, while the 1D mesh probe demonstrated regions where the 1D longitudinal elements were compressed to dense structures within the boundaries defined by the needle OD.

We characterized the cross-sectional diameters of the lowest-$D_t$ 2D and 1D probes post-injection as a function of needle ID/OD to quantify the differences mentioned above. A summary of these data (Figure 4c) shows several key results. 2D probes injected using the standard needle size (400 $\mu$m/650 $\mu$m ID/OD) yielded a distribution of probe diameters with a median of 270 $\mu$m. This value is ~40% of the injection needle OD and suggests substantial relaxation of the hydrogel brain tissue mimic upon removal of the injection needle. The diameters of the 2D probes implanted using 150 $\mu$m/250 $\mu$m and 100 $\mu$m/170 $\mu$m needles exhibited post-injection diameters much closer to the needle OD with median values and percentages of injection needle ODs of 202 $\mu$m and 80% and 185 $\mu$m and 109%, respectively. Differences in 2D cross-sectional diameter were statistically significant between the 400 $\mu$m/650 $\mu$m and 150 $\mu$m/250 $\mu$m injections ($P < 0.01$) in addition to the 400 $\mu$m/650 $\mu$m and 100 $\mu$m/170 $\mu$m injections ($P < 0.001$); however, the 2D 150 $\mu$m/250 $\mu$m and 100 $\mu$m/170 $\mu$m injections were not statistically significantly different ($P > 0.05$). On the other hand, the cross-sectional diameters of the 1D probes implanted using 150 $\mu$m/250 $\mu$m and 100 $\mu$m/170 $\mu$m needles exhibited median diameters and percentages of OD of 137 $\mu$m and 55% and 96 $\mu$m and 57%, respectively, thus showing a greater and statistically significant reduction in diameter and occupied volume compared to those of the corresponding 2D probes ($P < 0.0001$ in both 2D vs 1D cases).

To further explore these observations, we prepared 0.14% agarose hydrogel as a mimic of the vitreous humor of the eye,[38] given recent studies in which mesh electronics probes have been injected onto the concave surface of the retina cup.[33] Optical images of the lowest-$D_t$ 2D and 1D probes post-implantation (Figure S3) showed that in this hydrogel the lowest-$D_t$ 2D and 1D probes have diameters and conformations consistent with the needle OD or even expand beyond the OD, which contrasts the results in the more dense brain tissue-mimicking hydrogel.

Lastly, we characterized the structures of the lowest-$D_t$ 2D and 1D probes implanted into the brains of mice for different ID/OD injection needles (Figure 4d). The mesh probes were implanted to a depth of 4 mm using the FoV method;[28] then, mice were euthanized, and the brains fixed 1 h following mesh injection to provide a view of the acute probe/tissue structure (Materials and Methods in the Supporting Information). Microcomputed tomography (micro-CT) images (Figure 4e and Figure S4) highlight several key features. Overall, these images all appear to be similar to the only slightly greater transverse spread observed for 2D versus 1D probes injected through the 150 $\mu$m/250 $\mu$m and 100 $\mu$m/170 $\mu$m needles. Measurements of the cross-sectional diameters from these images are summarized in Figure 4f and reveal several key results. First, the injection of the 2D probes demonstrated consistent cross-sectional diameters for the 400 $\mu$m/650 $\mu$m, 150 $\mu$m/250 $\mu$m, and 100 $\mu$m/170 $\mu$m, needles with median mesh diameters and percentage of needle ODs of 213 $\mu$m and 33%, 220 $\mu$m and 88%, and 215 $\mu$m and 127%, respectively. Differences in the 2D cross-sectional diameters were not statistically significant for the 400 $\mu$m/650 $\mu$m, 150 $\mu$m/250 $\mu$m, and 100 $\mu$m/170 $\mu$m needles ($P > 0.05$ in all cases). Second, the significant transverse compression post-injection of the lowest-$D_t$ 2D probes, relative to needle OD, found from injection using the 400 $\mu$m/650 $\mu$m needles was not observed for the reduced diameter needles. Third, the 1D probes injected through 150 $\mu$m/250 $\mu$m and 100 $\mu$m/170 $\mu$m needles had median mesh diameters and percentages of needle ODs of 167 $\mu$m and 67% and 134 $\mu$m and 79%, respectively, thus showing compression relative to needle OD compared to 2D probes. Statistical analyses of these data show that the 1D compression relative to the corresponding 2D probes is statistically significant for both the 150 $\mu$m/250 $\mu$m ($P < 0.001$) and 100 $\mu$m/170 $\mu$m ($P < 0.0001$) needles studied. These results show that the substantial tissue relaxation following removal of the larger 400 $\mu$m/650 $\mu$m needles from the brain post-implantation is largely eliminated with the 2.6- and 3.8-fold smaller diameter needles. Additionally, the presence of transverse elements in the ultraflexible 2D mesh probes is important for avoiding compression of the longitudinal sensing elements as observed in 1D probes. We suggest that mesh electronics conformational volumes that are commensurate with injection needle OD allow for optimal probe integration with and electrode sampling of the tissue as opposed to a volume smaller than that perturbed during injection, which was observed with the largest needles for 2D probes and smaller needles for 1D probes. Lastly, we note that the injection of the lowest-$D_t$ 2D and 1D probes through the 150 $\mu$m/250 $\mu$m or 100 $\mu$m/170 $\mu$m needles required only 15.7 ± 1.8 or 21.1 ± 1.6 $\mu$L, respectively, which is significantly smaller than 100 $\mu$L volumes reported previously.[28−31]

In conclusion, we have demonstrated that we can rationally design mesh electronics to enable facile loading into and



DOI: 10.1021/acs.nanolett.9b01727
Nano Lett. 2019, 19, 4180−4187

ejection from capillary needles with IDs 4-fold smaller than those previously attainable and with reduced injection volumes. These results suggest substantial opportunity for applications in brain mapping where smaller diameter injection needles could reduce acute damage to native neural circuitry. Finally, we note that the reduced diameter implantation needles for mesh electronics implantation could extend the capabilities of this exciting probe technology to chronic scientific and clinical applications such as enabling targeting of sensitive nervous tissue, including rodent spinal cord, which would otherwise be precluded by more invasive probes and delivery mechanisms.

## ■ ASSOCIATED CONTENT

### Supporting Information

The Supporting Information is available free of charge on the ACS Publications website at DOI: 10.1021/acs.nanolett.9b01727.

Materials and Methods, fabricated ultraflexible mesh electronics (Figure S1), loading of mesh probes into glass capillary needles (Figure S2), injection of ultraflexible mesh electronics into vitreous humor mimic hydrogel (Figure S3), microcomputed tomography of mesh electronics in brain tissue (Figure S4), and supplementary references (PDF)

## ■ AUTHOR INFORMATION


### Corresponding Author

*E-mail: cml@cmliris.harvard.edu.

### ORCID

Charles M. Lieber: 0000-0002-6660-2456


### Author Contributions

⊥R.D.V. and T.Z. contributed equally to this work.

### Notes

The authors declare no competing financial interest.

## ■ ACKNOWLEDGMENTS

C.M.L. acknowledges support of this work by National Institutes of Health Director's Pioneer Award 1DP1EB025835-01, Air Force Office of Scientific Research Grant FA9550-14-1-0136, a Harvard University Physical Sciences and Engineering Accelerator award, and a Cutting-Edge Basic Research Award under National Institutes of Health/National Institute on Drug Abuse Grant 3R21DA043985-02S1. This material is based upon work supported by the National Science Foundation Graduate Research Fellowship Program under Grants DGE1144152 and DGE1745303 (R.D.V.). G.H. acknowledges support of this work by American Heart Association Postdoctoral Fellowship 16POST27250219 and National Institutes of Health Pathway to Independence Award from the National Institute on Aging (1K99AG056636-01). This work was performed in part at the Harvard University Center for Nanoscale Systems (CNS), a member of the National Nanotechnology Coordinated Infrastructure Network (NNCI), which is supported by the National Science Foundation.

## ■ REFERENCES


(1) Tian, B.; Liu, J.; Dvir, T.; Jin, L.; Tsui, J. H.; Qing, Q.; Suo, Z.; Langer, R.; Kohane, D. S.; Lieber, C. M. *Nat. Mater.* **2012**, *11*, 986–994.

(2) Liu, J.; Xie, C.; Dai, X.; Jin, L.; Zhou, W.; Lieber, C. M. *Proc. Natl. Acad. Sci. U. S. A.* **2013**, *110*, 6694–6699.

(3) Luan, L.; Wei, X.; Zhao, Z.; Siegel, J. J.; Potnis, O.; Tuppen, C. A.; Lin, S.; Kazmi, S.; Fowler, R. A.; Holloway, S.; Dunn, A. K.; Chitwood, R. A.; Xie, C. *Sci. Adv.* **2017**, *3*, No. e1601966.

(4) Dai, X.; Hong, G.; Gao, T.; Lieber, C. M. *Acc. Chem. Res.* **2018**, *51*, 309–318.

(5) Jiang, Y.; Tian, B. *Nat. Rev. Mater.* **2018**, *3*, 473–490.

(6) Rastogi, S. K.; Kalmykov, A.; Johnson, N.; Cohen-Karni, T. *J. Mater. Chem. B* **2018**, *6*, 7159–7178.

(7) Zhang, J.; Liu, X.; Xu, W.; Luo, W.; Li, M.; Chu, F.; Xu, L.; Cao, A.; Guan, J.; Tang, S.; Duan, X. *Nano Lett.* **2018**, *18*, 2903–2911.

(8) Hong, Y. J.; Jeong, H.; Cho, K. W.; Lu, N.; Kim, D. H. *Adv. Funct. Mater.* **2019**, *29*, 1808247.

(9) Jackson, A.; Fetz, E. E. *J. Neurophysiol.* **2007**, *98*, 3109–3118.

(10) Schwarz, D. A.; Lebedev, M. A.; Hanson, T. L.; Dimitrov, D. F.; Lehew, G.; Meloy, J.; Rajangam, S.; Subramanian, V.; Ifft, P. J.; Li, Z.; Ramakrishnan, A.; Tate, A.; Zhuang, K. Z.; Nicolelis, M. A. L. *Nat. Methods* **2014**, *11*, 670–676.

(11) Scholvin, J.; Kinney, J. P.; Bernstein, J. G.; Moore-Kochlacs, C.; Kopell, N.; Fonstad, C. G.; Boyden, E. S. *IEEE Trans. Biomed. Eng.* **2016**, *63*, 120–130.

(12) Berényi, A.; Somogyvári, Z.; Nagy, A. J.; Roux, L.; Long, J. D.; Fujisawa, S.; Stark, E.; Leonardo, A.; Harris, T. D.; Buzsáki, G. *J. Neurophysiol.* **2014**, *111*, 1132–1149.

(13) Son, D.; Lee, J.; Qiao, S.; Ghaffari, R.; Kim, J.; Lee, J. E.; Song, C.; Kim, S. J.; Lee, D. J.; Jun, S. W.; et al. *Nat. Nanotechnol.* **2014**, *9*, 397–404.

(14) Tee, B. C. K.; Chortos, A.; Berndt, A.; Nguyen, A. K.; Tom, A.; McGuire, A.; Lin, Z. C.; Tien, K.; Bae, W.-G.; Wang, H.; Mei, P.; Chou, H.-H.; Cui, B.; Deisseroth, K.; Ng, T. N.; Bao, Z. *Science* **2015**, *350*, 313–316.

(15) Imani, S.; Bandodkar, A. J.; Mohan, A. V.; Kumar, R.; Yu, S.; Wang, J.; Mercier, P. P. *Nat. Commun.* **2016**, *7*, 11650.

(16) Timko, B. P.; Cohen-Karni, T.; Yu, G.; Qing, Q.; Tian, B.; Lieber, C. M. *Nano Lett.* **2009**, *9*, 914–918.

(17) Sekitani, T.; Yokota, T.; Kuribara, K.; Kaltenbrunner, M.; Fukushima, T.; Inoue, Y.; Sekino, M.; Isoyama, T.; Abe, Y.; Onodera, H.; Someya, T. *Nat. Commun.* **2016**, *7*, 11425.

(18) Kim, D.-H.; Viventi, J.; Amsden, J. J.; Xiao, J.; Vigeland, L.; Kim, Y.-S.; Blanco, J. A.; Panilaitis, B.; Frechette, E. S.; Contreras, D.; Kaplan, D. L.; Omenetto, Y. H.; Huang, Y.; Hwang, K.-C.; Zakin, M. R.; Litt, B.; Rogers, J. A. *Nat. Mater.* **2010**, *9*, 511–517.

(19) Khodagholy, D.; Doublet, T.; Quilichini, P.; Gurfinkel, M.; Leleux, P.; Ghestem, A.; Ismailova, E.; Hervé, T.; Sanaur, S.; Bernard, C.; Malliaras, G. G. *Nat. Commun.* **2013**, *4*, 1575.

(20) Poldrack, R. A.; Farah, M. J. *Nature* **2015**, *526*, 371–379.

(21) Gong, Y.; Huang, C.; Li, J. Z.; Grewe, B. F.; Zhang, Y.; Eismann, S.; Schnitzer, M. J. *Science* **2015**, *350*, 1361–1366.

(22) Polikov, V. S.; Tresco, P. A.; Reichert, W. M. *J. Neurosci. Methods* **2005**, *148*, 1–18.

(23) Lacour, S. P.; Courtine, G.; Guck, J. *Nat. Rev. Mater.* **2016**, *1*, 16063.

(24) Hong, G.; Yang, X.; Zhou, T.; Lieber, C. M. *Curr. Opin. Neurobiol.* **2018**, *50*, 33–41.

(25) Hong, G.; Viveros, R. D.; Zwang, T. J.; Yang, X.; Lieber, C. M. *Biochemistry* **2018**, *57*, 3995.

(26) Feiner, R.; Dvir, T. *Nat. Rev. Mater.* **2017**, *3*, 17076.

(27) Liu, J.; Fu, T.-M.; Cheng, Z.; Hong, G.; Zhou, T.; Jin, L.; Duvvuri, M.; Jiang, Z.; Kruskal, P.; Xie, C.; Suo, Z.; Fang, Y.; Lieber, C. M. *Nat. Nanotechnol.* **2015**, *10*, 629–636.

(28) Hong, G.; Fu, T.-M.; Zhou, T.; Schuhmann, T. G.; Huang, J.; Lieber, C. M. *Nano Lett.* **2015**, *15*, 6979–6984.

(29) Fu, T.-M.; Hong, G.; Zhou, T.; Schuhmann, T. G.; Viveros, R. D.; Lieber, C. M. *Nat. Methods* **2016**, *13*, 875–882.

(30) Zhou, T.; Hong, G.; Fu, T.-M.; Yang, X.; Schuhmann, T. G.; Viveros, R. D.; Lieber, C. M. *Proc. Natl. Acad. Sci. U. S. A.* **2017**, *114*, 5894–5899.




DOI: 10.1021/acs.nanolett.9b01727
*Nano Lett.* 2019, 19, 4180–4187

(31) Schuhmann, T. G., Jr.; Yao, J.; Hong, G.; Fu, T.-M.; Lieber, C. M. *Nano Lett.* **2017**, *17*, 5836−5842.
(32) Fu, T.-M.; Hong, G.; Viveros, R. D.; Zhou, T.; Lieber, C. M. *Proc. Natl. Acad. Sci. U. S. A.* **2017**, *114*, E10046−E10055.
(33) Hong, G.; Fu, T.-M.; Qiao, M.; Viveros, R. D.; Yang, X.; Zhou, T.; Lee, J. M.; Park, H.-G.; Sanes, J. R.; Lieber, C. M. *Science* **2018**, *360*, 1447−1451.
(34) Yang, X.; Zhou, T.; Zwang, T. J.; Hong, G.; Zhao, Y.; Viveros, R. D.; Fu, T.-M.; Gao, T.; Lieber, C. M. *Nat. Mater.* **2019**, *18*, 510.
(35) Nemani, K. V.; Moodie, K. L.; Brennick, J. B.; Su, A.; Gimi, B. *Mater. Sci. Eng., C* **2013**, *33*, 4453−4459.
(36) Chen, Z.-J.; Gillies, G. T.; Broaddus, W. C.; Prabhu, S. S.; Fillmore, H.; Mitchell, R. M.; Corwin, F. D.; Fatouros, P. P. *J. Neurosurg.* **2004**, *101*, 314−322.
(37) Ahearne, M.; Yang, Y.; El Haj, A. J.; Then, K. Y.; Liu, K.-K. *J. R. Soc., Interface* **2005**, *2*, 455−463.
(38) Nickerson, C. S.; Karageozian, H. L.; Park, J.; Kornfield, J. A. *Invest. Ophthalmol. Visual Sci.* **2004**, *45*, 37.



DOI: 10.1021/acs.nanolett.9b01727
*Nano Lett.* 2019, 19, 4180−4187